Solar wind driven variations of electron plasma sheet densities and temperatures beyond geostationary orbit during storm times

S. Dubyagin[1], N. Yu. Ganushkina[1,2], I. Sillanpää[1], A. Runov[3]

Corresponding author: S. Dubyagin, Finnish Meteorological Institute, POBox 503, Helsinki, FIN-00101, Finland/(Stepan.Dubyagin@fmi.fi)

[1]Finnish Meteorological Institute, Helsinki, Finland.

[2]Climate and Space Sciences and Engineering Department, University of Michigan, Ann Arbor, MI, USA.

[3]Institute of Geophysics and Planetary Physics, University of California, Los Angeles, USA.

This article has been accepted for publication and undergone full peer review but has not been through the copyediting, typesetting, pagination and proofreading process, which may lead to differences between this version and the Version of Record. Please cite this article as doi: 10.1002/2016JA022947

Abstract. The empirical models of the plasma sheet electron temperature and density on the nightside at distances between 6 and 11 R_E are constructed based on Time History of Events and Macroscale Interactions During Substorms (THEMIS) particle measurements. The data set comprises ~400 hours of observations in the plasma sheet during geomagnetic storm periods. The equatorial distribution of the electron density reveals a strong earthward gradient and a moderate variation with magnetic local time symmetric with respect to the midnight meridian. The electron density dependence on the external driving is parameterized by the solar wind proton density averaged over 4 hours and the southward component of interplanetary magnetic field (IMF B_S) averaged over 6 hours. The interval of the IMF integration is much longer than a typical substorm growth phase and it rather corresponds to the geomagnetic storm main phase duration. The solar wind proton density is the main controlling parameter but the IMF B_S becomes of almost the same importance in the near-Earth region. The root-mean-square deviation between the observed and predicted plasma sheet density values is 0.23 cm^{-3} and the correlation coefficient is 0.82. The equatorial distribution of the electron temperature has a maximum in the post-midnight – morning MLT sector, and it is highly asymmetric with respect to the local midnight. The electron temperature model is parameterized by solar wind velocity (averaged over 4 hours), IMF B_S (averaged over 45 min), and IMF B_N (northward component of IMF, averaged over 2 hours). The solar wind velocity is a major controlling parameter and IMF B_S and B_N are compara-

ble in importance. In contrast to the density model, the electron temperature shows higher correlation with the IMF B_S averaged over ∼45 min (substorm growth phase time scale). The effect of B_N manifests mostly in the outer part of the modelled region ($r > 8R_E$). The influence of the IMF B_S is maximal in the midnight – post-midnight MLT sector. The correlation coefficient between the observed and predicted plasma sheet electron temperature values is 0.76 and the root-mean-square deviation is 2.6 keV. Both models reveal better performance in the dawn MLT sector.

1. Introduction

The distributions of low energy electrons (below 200-300 keV) and their variations in the near-Earth plasma sheet, at distances beyond geostationary orbit, have not sufficiently been studied in detail. Yet, this population is critically important for magnetospheric dynamics, especially during storm times. One obvious example is their role as the seed population, being further accelerated to MeV energies by various processes in the Earth's radiation belts. Several modeling attempts have been made [*Jordanova and Miyoshi*, 2005; *Miyoshi et al.*, 2006; *Chen et al.*, 2006; *Jordanova et al.*, 2014]. The electron flux at these low energies is largely determined by convective and substorm-associated electric fields and varies significantly with geomagnetic activity driven by the solar wind [*Mauk and Meng*, 1983; *Kerns et al.*, 1994; *Liemohn et al.*, 1998; *Ganushkina et al.*, 2013, 2014]. Inward electron transport includes also radial diffusion and excites plasma wave instabilities that give rise to local electron acceleration and electron precipitation into the atmosphere. Transport and loss processes are far from being understood at present. It should be also noted that the electron flux at these energies is important for spacecraft surface charging [*Garrett*, 1981; *Lanzerotti et al.*, 1998; *Davis et al.*, 2008; *Thomsen et al.*, 2013].

There has been a number of studies on low energy electrons at geostationary orbit. *Korth et al.* [1999]; *Denton et al.* [2005]; *Sicard-Piet et al.* [2008]; *Denton et al.* [2015] concentrated mainly on the analysis of LANL MPA and SOPA electron data. *Friedel et al.* [2001] analyzed the electron data from the Polar Hydra instrument and *Kurita et al.* [2011] the data from the THEMIS spacecraft. None of the studies produced solar wind

driven empirical relations for electron fluxes or moments of electron distribution function which can be used easily for radiation belt modeling.

In the near-Earth plasma sheet, continuous measurements of plasma sheet electrons are not available, in contrast to geostationary orbit. Numerous studies addressed the magnetospheric plasma transport and sources [*Terasawa et al.*, 1997; *Borovsky et al.*, 1998a, b; *Wing and Newell*, 2002]. There have been several statistical models for plasma sheet electrons derived from GEOTAIL and CLUSTER data, such as, for example, *Åsnes et al.* [2008]; *Burin des Roziers et al.* [2009]. *Artemyev et al.* [2013] analyzed the electron temperature radial distribution in the magnetotail using THEMIS observations at $r > 10R_E$. These studies are not models with empirical relations which can be used for real event modeling by the wider scientific community.

Only two empirical models of the plasma sheet plasma parameters have been presented since 2000. These models are *Tsyganenko and Mukai* [2003] and *Sergeev et al.* [2015]. The *Tsyganenko and Mukai* [2003] model is the only model, where an analytical description of the plasma was derived for a 2D distribution of the central plasma sheet ion temperature T_i, density n_i and pressure p_i as functions of the incoming solar wind and interplanetary magnetic field parameters at distances of 10-50 R_E based on Geotail data. *Sergeev et al.* [2015] presented the correlations between 1-h-averaged central plasma sheet and solar wind (and AL index) parameters based on THEMIS data but they were not derived for storm times.

Ganushkina et al. [2013, 2014, 2015] modeled the electron transport from the plasma sheet to the geostationary orbit setting the boundary at 10 R_E as a kappa distribution with the parameters of number density n_e and temperature T_e in the plasma sheet given

by *Tsyganenko and Mukai* [2003]. In *Ganushkina et al.* [2013, 2014, 2015], the electron n_e is assumed to be the same as that for ions and $T_e/T_i = 0.2$ is taken into account (which relation was shown, for example, in *Kaufmann et al.* [2005] and *Wang et al.* [2012], based on Geotail and THEMIS data). A time shift of 2 h following *Borovsky et al.* [1998b] for the solar wind material to reach the midtail plasma sheet is also introduced. Applying *Tsyganenko and Mukai* [2003] model for boundary conditions for electrons has a number of serious limitations. This model was derived from Geotail data for ions. According to the studies based on THEMIS data analysis [*Wang et al.*, 2012], the ratio T_e/T_i can vary during disturbed conditions. Moreover, at distances closer than 10 R_E, it can happen that the correlation between T_i and T_e does not exist at all and no certain ratio can be determined [*Runov et al.*, 2015].

The paper presents the empirical model of the electron plasma sheet densities and temperatures derived from the THEMIS [*Angelopoulos*, 2008a] data. Sections 2 and 3 contain the detailed description of the data we have selected and analyzed. Section 4 demonstrates the methodology of determining the model input parameters. Section 5 presents the empirical relations for electron plasma sheet density and temperature. The results of the study are discussed in Section 6. The goal of Section 7 is to validate the model performance and Section 8 presents the conclusions.

2. The Data Sources

This study relies on the data of the Time History of Events and Macroscale Interaction during Substorms (THEMIS) mission [*Angelopoulos*, 2008a]. The mission was launched on February 17, 2007, and it comprises five identical probes on elliptical, nearly-equatorial orbits. Each of the probes has among other scientific instruments two particle

instruments, namely, Electrostatic Analyser (ESA) [*McFadden et al.*, 2008a] to measure the ion and electron distribution functions over the energy range from a few eV up to 25 (30) keV for ions (electrons) on each spin period ($\sim$ 3 sec.) and Solid State Telescope (SST) [*Angelopoulos et al.*, 2008b] to measure ion and electron distributions over energies from 25 keV up to first MeVs on each spin period. We also used the spin resolution Flux Gate Magnetometer (FGM) data [*Auster et al.*, 1991]. All aforementioned data and the calibrating procedures are publicly available at the THEMIS mission web site (http://themis.ssl.berkeley.edu/index.shtml)

In this study we used solar wind and IMF data from the OMNI database from the GSFC/SPDF OMNIWeb interface at http://omniweb.gsfc.nasa.gov. 5-min. resolution data were used as input parameters for magnetotail neutral sheet model [*Tsyganenko and Fairfield*, 2004] and 1-min. resolution data were used for computation of the input parameters for our empirical model of electron temperature and density.

Finally, the 1-min. resolution SYM-H index was downloaded from World Data Center for geomagnetism, Kyoto (http://wdc.kugi.kyoto-u.ac.jp/).

3. Selection of data intervals

We have analyzed the data from the particle detectors onboard the THEMIS probes P3, P4, P5 (D, E, A) during geomagnetic storms which took place through 2007–2013. All observations came from the region on the nightside at distances r = 6–11 R_E. The major axes of the orbits for all probes were aligned so that the probes were clustered closely during their apogees at r =10–12 R_E. However, in this study we did not use the advantage of a multi-spacecraft mission and consider the measurements at different

spacecraft as independent data records. The probe separation in this region was typically ~ 0.03–$2R_E$ except for year 2013 when the separation varied between 2 and $8R_E$.

Storm periods were of a special interest for our study, since the solar wind driving as well as the magnetospheric plasma parameters can reach extreme values and all the dependencies as well as their saturation levels can manifest more clearly. For this reason, we selected all the periods with $SYM - H < -50$ nT and one day before and one day after these periods for almost whole THEMIS mission lifetime 2007–2013. This selection also includes the quiet periods before the storms.

When studying the distribution of the plasma parameters in the equatorial plane, it is important to make sure that a probe was in very center of the plasma sheet (near the magnetotail current neutral sheet) to refer the measurements to a particular radial distance. To control the spacecraft position relative to the neutral sheet we use two step selection: (1) Select all periods when the probes are within 1.5 R_E from the neutral sheet predicted by *Tsyganenko and Fairfield* [2004] model; (2) Using THEMIS magnetic field measurements we select only measurements when $|B_n| > |B_t|$, where B_n and B_t are the magnetic field components normal and tangential to the model neutral sheet. Such approach is very robust and it has been successfully applied to the THEMIS data [*Dubyagin et al.*, 2010]. This selection procedure was applied to THEMIS data when P3, P4, P5 (D, E, A) probes were at $R = 6$–$11R_E$.

Although the combined distribution function covers the energy range up to 3 MeV, we only used the data in the 30 eV – 300 keV energy range. The 30 eV low energy limit is chosen so as to eliminate the possible contribution of photoelectrons in case the spacecraft potential is evaluated incorrectly. The electron and ion moments were computed

from combined (ESA and SST) distribution function using updated calibration procedures (including ESA background contamination and SST sun contamination removal, software version dated December 2015). However, even after all calibration procedures are applied, the penetrating background may not be fully removed. As an additional test of the data accuracy, we compare the densities measured by the ion and electron detectors. The readers are referred to *McFadden et al.* [2008b] for more details on the ESA performance issues.

Depending on ESA and SST mode, the combined plasma moments are available at spin resolution or only at $\sim$ 96 second resolution. When the 3-second resolution moments were available, it was convenient to average them over 96 sec intervals (1.6 minute) to get combined data set with uniform time resolution. It should be noted that the measurements at 96-sec resolution were not accumulated values but instant distributions (accumulated during one spacecraft spin period). For this reason, these data are expected to reveal more scatter and we do not use them for model construction. This data set was used only for verification of the models.

After synchronization with the solar wind data, we obtained $\sim 83,000$ data records with $\sim$ 1.6-min resolution $\sim 63,000$ of which are obtained from the spin-resolution data. Since the quasi-neutrality holds in the magnetospheric plasma, the quality of the plasma moments can be checked comparing the densities computed from electron (N_e) and ion (N_i) measurements. It turned out that significant part of the data shows discrepancies between N_e and N_i. In majority of these anomalous events, N_i exceeds N_e. We analyzed these events and found that typically cold dense plasma with energies $\leq$ 100 eV can be seen right above the low energy limit. It is likely that some part of this cold population is cut

off by low energy limit and the fraction of the cut off population is different for the ion and electron distributions. This leads to discrepancy between N_e and N_i measurements. We also found that a vast majority of these events occurred in the 18–24 MLT sector during the periods with very weak geomagnetic activity. This finding is also in agreement with our hypothesis because a cold plasma of the plasmasphere can extend to larger geocentric distances during such periods especially in the dusk-to-midnight sector. Although these data potentially can be used in the future studies, if the presence of multiple populations in the particle distribution is properly addressed, in the present study we discard all measurements which do not satisfy the condition $N_i/1.5 < N_e < 1.5N_i$. This procedure reduced the size of our statistics by one third. Although this criterion seems to be rather weak, it is justified because, during storm time, the ion data are expected to be less accurate in comparison to the electron data due to a contamination from heavier ions and larger gap between ESA and SST energy ranges (especially for late years).

Finally, our data set consists of $\sim 45,000$ records obtained from the spin resolution measurements and $\sim 12,000$ obtained from $\sim$ 1.6-min resolution measurements. Hereafter, we will refer to these data sets as a "primary" and "auxiliary" data sets, respectively. Table 1 shows the number of samples in the data sets for every year during the THEMIS mission. The primary data set includes only data starting from the year 2010 while the years 2007–2009 contribute 20% to the auxiliary data set. Figure 1a shows the distribution of the points corresponding to the primary data set in the XY_{GSM} plane (only every tenth point is shown). The colors correspond to different SYM-H index ranges. The strong dusk-dawn asymmetry can be seen in the figure. Although moderate asymmetry existed in the original data set (probably owning to orbital/seasonal effect), so promi-

nent lack of the data points in the dusk sector is mostly due to removal of the data with $N_i \neq N_e$. Though not immediately obvious from this dense distribution of points, the dawn-dusk asymmetry exists only for the moderate SYM-H subsets and disappears for SYM-H< -50 nT.

It is worth comparing these datasets with datasets used in the previous studies. *Tsyganenko and Mukai* [2003] used Geotail data and their dataset comprised 7234 1-min records ($\sim$ 120 hours). Since we used 1.6-min resolution data, the size of our dataset should be multiplied by factor 1.6 to compare with *Tsyganenko and Mukai* [2003] dataset. However, we used observations onboard three probes clustered closely. For this reason, the size of our dataset should be divided by 3 (this estimate is a bit pessimistic because the probe separation can be as large as $\sim 9R_E$). After this normalization, our dataset size corresponds to $\sim$ 400 hours of observations. *Wang et al.* [2006] apparently used the same data set as *Tsyganenko and Mukai* [2003]. *Sergeev et al.* [2015] use 4500–5000 hourly averaged measurements onboard three THEMIS probes on the nightside 21–06 MLT $r = 9$–$12R_E$. After dividing by 3, to take into account simultaneous measurements at three probes, the data set size is 1500–1600 h, which is four times larger than data set used in the present study. However, *Sergeev et al.* [2015] use only data from ESA spectrometer in 5 eV–25 keV energy range and there is no spatial dependence included in the model.

4. Solar wind driven model for electron plasma sheet densities and temperatures: Input parameters

4.1. Methodology

The macroscopic plasma parameters in the near-Earth magnetotail are affected by multiple factors. Among them, there are the magnetic configuration change (it affects

the plasma parameters through the adiabatic compression of the magnetic flux tubes) [*Borovsky et al.*, 1998b; *Dubyagin et al.*, 2010; *Artemyev et al.*, 2013], the substorm cycle (arrival of a new hot tenuous plasma from the distant magnetotail during the main phase) [*Sergeev et al.*, 2015], the variations of the magnetosheath plasma parameters (since the magnetosheath is a source of the plasma sheet material) [*Terasawa et al.*, 1997; *Borovsky et al.*, 1998a; *Wang et al.*, 2010], and the variation of the magnetotail plasma transport modulated by the dayside reconnection rate. To make it even more complicated, the regions and mechanisms of the magnetosheath plasma penetration into the magnetotail are different during periods of southward and northward IMF [*Wang et al.*, 2010]. In addition, all these factors affect the plasma sheet with different time lags and these delays can be different for different regions of the magnetotail [*Terasawa et al.*, 1997; *Borovsky et al.*, 1998a; *Wang et al.*, 2010]

To investigate the lag of the solar wind influence, every record of the plasma sheet electron density and temperature was accompanied by solar wind data containing 12 hour prehistory. In the OMNI database, the solar wind parameters are projected in time to the moment when solar wind reaches the estimated bow shock position. We estimate the shortest time for solar wind disturbance (seen in the OMNI data) to have an effect on the nightside inner magnetosphere to be $\sim$ 5 minutes. For every measurements in the plasma sheet taken at time t_0, the 12 hours period preceding the time $t_0 - 5$ min. was broken into 15 minute subintervals and solar wind parameters were averaged over these subintervals. That is, every measurement in the plasma sheet was complemented by 48 of 15-min averages of the solar wind parameters for the preceding 12 h interval.

As a first step, we binned the THEMIS observations according to the probe location in the plasma sheet. We used two discriminating parameters: a geocentric distance $r = (X^2+Y^2+Z^2)^{\frac{1}{2}}$ and an azimuth angle $\phi = \arctan(-Y_{GSM}/X_{GSM})$. We used two intervals of geocentric distance: $r = 6$–$8.5R_E$ and $r = 8.5$–$11R_E$, and three sectors of the azimuth angle: dawnside ($-90° < \phi < -30°$), central ($-30° < \phi < 30°$), and duskside ($30° < \phi < 90°$). These bins are shown in Figure 1b. We investigated the dependence of the electron plasma parameters on the solar wind parameters separately for each bin. Let P_k be a plasma sheet parameter and D_{ik} be a 15-min average of a solar wind parameter. Here k is the index corresponding to the plasma sheet measurements at the time t_k and $i = 1, ..., 48$ corresponds to the 15-min average preceding the time t_k by $\Delta t = 5 \text{ min} + i \cdot 15 \text{ min}$.

For $L = 1, ..., 48$ and for $M \leq 48 - L + 1$, we computed the following mean sums:

$$F(L, M, k) = \frac{\sum_{i=L}^{L+M-1} D_{ik}}{M}. \quad (1)$$

Here L represents the lag and M represents the duration over which the parameter is averaged.

These sums are equivalent to time integrals:

$$F(t_{lag}, \Delta T, t_k) = \frac{1}{\Delta T} \int_{t_k - t_{lag} - \Delta T}^{t_k - t_{lag}} D(t) dt. \quad (2)$$

The delays of the plasma sheet parameter response to the changes of the solar wind can be deduced from the analysis of the correlation coefficient between P_k and $F(L, M, k)$ for different L and M. These correlation coefficients can be plotted as function of L and M converted to the time units t_{lag} and ΔT.

Imagine an ideal system whose parameter P responds to the changes of some other parameter D with a fixed time lag t_r. The correlation between P and D would have a peak at $t_{lag} = t_r$ and $\Delta T = 0$. However, the correlation would still be high for nonzero ΔT as long as t_r is inside the interval of averaging ($t_{lag} < t_r < t_{lag} + \Delta T$) and ΔT is less than the autocorrelation time scale (T_{auto}) for D (that is, if an instant value of D can be approximated by its mean average over the time interval ΔT). The shaded area in Figure 2 shows the region satisfying the aforementioned conditions. Obviously, inside this region the correlation is highest when the interval of averaging is centered at t_r, that is $t_{lag} + \Delta T/2 = t_r$ (blue dashed line in Figure 2).

However, the parameters of the system do not necessarily depend on instant values (even if lagged) of the external drivers. For example, the magnetic flux in the magnetotail lobes better correlates with the time integrated solar wind geoeffective electric field than with its instant value [*Shukhtina et al.*, 2005]. In such a case, one can expect that correlation would be higher at some $\Delta T > 0$. In addition, in real magnetosphere the time lags obviously are not constant. It also leads to smearing out the correlation peak at $\Delta T = 0$ and an increase of the correlation at $\Delta T > 0$.

4.2. Input parameters for electron plasma sheet density model

Figure 3 shows the plots for correlation between the plasma sheet and the solar wind densities (all results in Sections 4.2–5 are obtained using primary data set). Figures 3a–f correspond to six spatial bins shown in Figure 1b. The horizontal axis corresponds to the time lag or index L in Equation 1. The vertical axis corresponds to the interval of averaging or index M in Equation 1. A color scale on the right side of each plot shows

the range of the linear correlation coefficients (C.C.). The black oblique lines correspond to $\Delta T_N = const - 2 \cdot t_N$ dependence (equivalent to blue dashed line in Figure 2).

There is an obvious similarity between these plots and Figure 2. The correlation maxima in Figures 3a, b, c, d are roughly organized along oblique lines, and the regions of enhanced correlation are delineated by lines $\Delta T_N = const - t_N$ on the left/bottom side in Figures 3a, c, d, f.

The plots on the left and right correspond to the dawn and dusk bins, respectively. It can be seen that the maximum correlation is found for the dawnside bins (C.C.≥ 0.70) and the correlation is higher for the outer bins (BIN 1–3 see Figure 1b). These results are in agreement with dusk-dawn asymmetry of the plasma transport from the magnetosheath found by *Wing et al.* [2005] and *Wang et al.* [2010], however, it is a bit counterintuitive taking into account the eastward direction of the electron magnetic drifts. The lag values are generally in agreement with those found by *Borovsky et al.* [1998a].

Table 2 presents the statistical properties of the data subsets for the different bins. First three lines represent the bin numeration and the coordinates. Forth line shows the number of 1.6-min resolution records in every bin. It can be seen that the most sparsely populated bin is BIN 6. Its data set comprises 2295 records. However, this number is misleading since the time-scales of the solar wind parameters variations are much longer than 1.6-min resolution of our data set. *Borovsky et al.* [1998a] obtained the following characteristic times-scales: ~ 1.5 h for IMF B_Z, ~ 10 h for solar wind density, and ~ 32 h for solar wind velocity (these scales are expected to be somewhat shorter for storm periods). To evaluate the size of our statistics more realistically, we searched through the database, counting separate 1-hour intervals containing at least one data point. We found 444 such intervals

for BIN 1 and 133 intervals for BIN 6. For 5-hour characteristic period, we found 181 intervals for BIN 1 and only 77 intervals for BIN 6. For this reason (and may be partly due to orbital/seasonal effect), the standard deviations of the solar wind parameters also show some variations from bin to bin. Bottom part of Table 2 shows the ranges of the standard deviations found for various lag values between 0 and 12 hours (the standard deviations were computed for 15-min resolution data). It can be seen that the variability of the solar wind parameters changes significantly for different time lag values inside a data subset for a single bin. It means that some dependencies seen in Figure 3 could be due to a limited size of the dataset since one can expect that the correlation between two quantities depends on the variability of the driving one. To rule out this possibility, we plotted additional figures (not shown) in the same format as Figure 3 but for a standard deviation (σ) of a corresponding solar wind parameter. Analyzing these figures, we found that the main features seen in Figures 3 are real (σ shows no or weak variation in that part of the figure).

Although the values of ΔT_N and t_N corresponding to the highest correlation obviously are different from bin to bin, we need to choose fixed values for a computation of the input parameters for the empirical models. We attempted to find a compromise so that the model works for all MLTs in r = 6–11R_E range. Keeping this in mind, t_N = 0.5 h and ΔT_N = 4 h were chosen. These values are marked by a black circle in all panels of Figure 3. However, it should be remembered that the confidence interval of these parameters is very broad (at least ±1 hour).

The model dependence on IMF is parameterized by southward (B_S) and northward (B_N) IMF components ($B_S = -B_Z^{IMF}$ if $B_Z^{IMF} < 0$ and $B_S = 0$ if $B_Z^{IMF} \geq 0$; $B_N = 0$

if $B_Z^{IMF} < 0$ and $B_N = B_Z^{IMF}$ if $B_Z^{IMF} \geq 0$). Figure 4 shows the plots of correlations between the plasma sheet electron density and IMF B_S. The format is the same as in Figure 3. In contrast to the solar wind density, the highest correlation between the B_S and plasma sheet electron density is found for the near-Earth bins. Surprisingly, highest correlations are found for relatively long intervals of averaging ΔT_{BS} = 2–6 h. This is much longer than typical substorm growth phase duration. It could be due to strong variations of the lag in the real system, but in such a case one would expect weaker correlation. We will discuss the possible reasons for this in Section 7. We chose the $t_{BS} = 0.5$ h and $\Delta T_{BS} = 6$ h. The lag was chosen so to be the same as that for solar wind density parameter (and it will be shown later that 0.5 h lags are reasonable choice for all temperature model parameters too).

Table 3 summarizes the results presented in this section. When comparing the top and bottom parts of the Table 3, it can be seen that introducing a time lag to the input parameter can significantly improve the correlations. We have also checked a few more solar wind and IMF parameters (not shown). However, even if the correlations were comparable to those for N_{SW}, B_S and B_N, the resulting model quality (gauged by correlation between the model predictions and the data, see Section 7) was worse and we discarded them in the present version of the model. For example, motivated by the fact that the solar wind - magnetotail plasma transport characteristic time is different for the intervals southward and northward IMF B_Z, we introduced two parameters $N_{SW}^{(S)}$ and $N_{SW}^{(N)}$. $N_{SW}^{(S)} = N_{SW}$ when IMF $B_Z < 0$ and $N_{SW}^{(S)} = 0$ when IMF $B_Z > 0$. $N_{SW}^{(N)}$ is defined in an opposite way. Although the lag-duration plots for $N_{SW}^{(S)}$ and $N_{SW}^{(N)}$ showed plausible patterns, the resulting quality of the electron density model was worse.

It can be noticed that northward component of IMF shows a bit worse correlation with the plasma sheet density than southward component (Table 3). It turned out that discarding IMF B_N from the list of input parameters leads to only minor reduction of the density model quality. For this reason, and for the sake of simplicity, we have left only two input parameters N_{SW} and B_S in our density model.

4.3. Input parameters for electron plasma sheet temperature model

Table 4 shows the correlation between the plasma sheet electron perpendicular temperature (T_e) and solar wind parameters. It can be seen that solar wind velocity exhibits strongest correlation. Similar results have been found for plasma sheet ion temperature [*Borovsky et al.*, 1998a; *Tsyganenko and Mukai*, 2003]. The lowest correlations are obtained for the duskside bins. It can also be noticed that IMF B_S and B_N affect the electron temperature in an opposite way. Figure 5 shows the correlations between T_e and V_{SW} for six spatial bins in the same format as in Figure 3. The correlations show very weak dependence on t_V and ΔT_V for several bins. It is an expected result since the solar wind velocity autocorrelation characteristic time scale is largest of all solar wind parameters (See Figure 6 in *Borovsky et al.* [1998a]). We chose $t_V = 0.5$ h and $\Delta T_V = 4$ h.

Figure 6 shows the similar correlation plots for IMF B_S. There is no clear dependence on MLT. Although for some bins the correlation is rather weak, the duration and the lag at the correlation peak fit well the substorm timescales (0.5–2 hours). We chose the time lag $t_{BS} = 30$ minutes which can be interpreted as the time needed for the lobe magnetic flux to start to influence the near-Earth magnetotail and the averaging interval $\Delta T_{BS} = 45$ minutes is close to the typical substorm growth phase duration.

Figure 7 shows the similar plots for IMF B_N. Color scale on the right side of each plot corresponds to the absolute value of the correlation coefficient. The highest correlation is on the dawnside. Surprisingly, the correlations are even higher than those for B_S. To make sure that these correlations are not due to the mutual correlation between IMF B_N and V_{SW}, we inspected the correlation between B_N and V_{SW} for various lags t_V and t_{BN} and found no significant correlation. We chose $t_{BN} = 0.5$ h and $\Delta T_{BN} = 2$ h.

5. Solar wind driven model for electron plasma sheet densities and temperatures: Empirical relations

Using the time constants given in Table 5, we computed the input parameters for the electron density and temperature models as time integrals in the form of Equation 2. Note that the lag values in Table 5 (0.58 h) are different from those determined in Sections 4.2 and 4.3 (0.5 h). The lag constants in Table 5 just take into account 5-min offset of the solar wind parameters used in this study (See Section 4.1).

At the first step, we use the following functional form of the plasma sheet parameter dependence on the solar wind input parameters:

$$P_{ps} = G_0(\phi, R) + \sum_{j=1,...} G_j(\phi, R) \cdot P_j^{SW}, \tag{3}$$

where P_j^{SW} are the corresponding solar wind parameters, and $G_j(\phi, R)$ are the 2nd order polynomials of an azimuth angle ϕ and radial distance R given as

$$G_j(\phi, R) = \sum_{m,n=0,1,2} C_{mnj} \cdot R^n \phi^m. \tag{4}$$

The polynomial coefficients C_{mnj} were found by fitting Equation 3 to the data (primary data set). After the first set of the coefficients was found, we computed the correlation coefficient between the plasma sheet parameters and the model predictions. Using this

correlation coefficient as a reference value, we started to remove more and more terms from Equation 3 (simplifying the polynomials) seeking for a minimal set of terms which still provide good model quality. That is, for every possible subset of the terms in Equation 3, we fitted this truncated model to the data and computed the correlation coefficient between the data and the model. Comparing this correlation coefficient with a reference one, we checked that such simplification of Equation 3 did not lead to significant reduction of the model quality. After this simplification was done, we introduced the nonlinear parameters (exponential powers of the driving parameters) and checked if this modification leads to significant improvement. The downhill simplex algorithm was used for finding a minimum of the error function [*Nelder and Mead*, 1965].

Applying this method to the plasma sheet electron density and temperature datasets, we come up with following solutions. The number density in the plasma sheet (N_{ps}) is given in cm^{-3} as follows:

$$N_{ps} = A_1 + A_2 R^* + A_3 \phi^{*2} R^* + A_4 \phi^{*2} + A_5 N^*_{sw} + (A_6 + A_7 R^*) B^*_S, \tag{5}$$

where, $\phi^* = \phi/90°$, $R^* = R/10R_E$ are normalized coordinates, and N^*_{sw}, B^*_S are the time-integrated and normalized parameters characterizing the external conditions and defined as:

$$N^*_{sw}(t_0) = \frac{1}{10\ \mathrm{cm}^{-3} \Delta T_N} \int_{t_0 - t_N - \Delta T_N}^{t_0 - t_N} N_{sw}(t) dt, \tag{6}$$

$$B^*_S(t_0) = \frac{1}{2\ \mathrm{nT}\ \Delta T_{BS}} \int_{t_0 - t_{BS} - \Delta T_{BS}}^{t_0 - t_{BS}} B_S(t) dt. \tag{7}$$

Here, N_{sw} and B_S are the solar wind density and southward IMF component. The values for t_N, ΔT_N, t_{BS} and ΔT_{BS} are given in Table 5 and the model coefficients A_i are given in Table 6. Figure 8a shows the electron density values observed by THEMIS probes versus the model predictions.

The temperature in the plasma sheet (T_{ps}) is given in keV as follows:

$$T_{ps} = [A_1 + A_2\phi^* + A_3 V_{sw}^* + (A_4 + A_5\phi^{*2} R^*) B_S^{*A_7} + A_6 R^* B_N^{*A_8}]^{A_9}, \tag{8}$$

where

$$V_{sw}^*(t_0) = \frac{1}{400 \text{ km/s } \Delta T_V} \int_{t_0 - t_V - \Delta T_V}^{t_0 - t_V} V(t) dt, \tag{9}$$

$$B_S^*(t_0) = \frac{1}{2 \text{ nT } \Delta T_{BS}} \int_{t_0 - t_{BS} - \Delta T_{BS}}^{t_0 - t_{BS}} B_S(t) dt, \tag{10}$$

$$B_N^*(t_0) = \frac{1}{2 \text{ nT } \Delta T_{BN}} \int_{t_0 - t_{BN} - \Delta T_{BN}}^{t_0 - t_{BN}} B_N(t) dt. \tag{11}$$

Here, V_{sw}, B_S, and B_N are the solar wind density and the southward and northward IMF components, respectively. The values for t_V, ΔT_V, t_{BS}, ΔT_{BS}, t_{BN} and ΔT_{BN} are given in Table 5 and the model coefficients A_i are given in Table 6. Figure 9a shows the electron temperature values observed by THEMIS probes versus the model predictions. It can be seen that for high electron temperatures, the THEMIS measurements typically exceed the model prediction. This bias would be much stronger if the standard least-squared error function is used. In order to minimize the bias, we have modified the error function as follows:

$$ERR = \sum_j W \cdot |T_j^{THM} - T_j^{model}| \quad (12)$$

Here, T_j^{THM} and T_j^{model} are the THEMIS measurements and model predictions, respectively, and weight coefficient W is a linear function of T_j^{THM} changing from 1 at $T_j^{THM} = 0$ to 1.5 at $T_j^{THM} = 22$ keV.

6. Solar wind driven model for electron plasma sheet densities and temperatures: Results

Some properties of the empirical electron plasma models becomes evident after inspection of Equations 5 and 8 and Table 6. The resulting density model is very simple. Only terms symmetric with respect to the midnight meridian remain after the model simplification as described in Section 5. The symmetry of the density distribution is an interesting finding since the storm time inner magnetosphere is highly asymmetric (at least during the main phase). The plasma sheet density response to changes of the solar wind density is positive and uniform across whole region of the model applicability. It is a bit surprising, but the plasma sheet electron density response to the southward IMF component is also positive. *Tsyganenko and Mukai* [2003] reported opposite dependence. However, it should be noted that the model is parameterized by B_S lagged by 0.5 h and averaged over six hours, that is, this density response is not related to the substorm cycle but rather to the geomagnetic storm time-scale. In addition, this response is strongest in the near-Earth region and disappears at $r = 11R_E$, where *Tsyganenko and Mukai* [2003] model's validity region begins. This IMF B_S effect can be interpreted as a result of the compression of the flux tube due to inflation of the inner magnetosphere magnetic configuration caused by the ring current strengthening. However, we can not be sure that this effect manifests

only during storm-times. Figures 10a and 10b show the distribution of the plasma density in the equatorial plane. The corresponding input parameters are given at the top of each panel. The density increases towards the Earth and peaks at midnight. Note that the model reveals opposite MLT dependence at the outer boundary of the region (the density is highest near the dusk and dawn meridians). This feature manifests more clearly in Figure 10a and it is in agreement with *Tsyganenko and Mukai* [2003] model (see their Figure 10).

Figures 10c–f show the equatorial maps of the electron temperature distributions for four combinations of the model input parameters. In contrast to the density distributions, the electron temperature exhibits very strong dusk-dawn asymmetry. Figure 10c shows the temperature distribution for $B_S^* = B_N^* = 0$. In fact, it is unlikely that such combination of the parameters occur in reality since it implies that transverse component of IMF is zero for at least 45 minutes (see Table 5). For these parameters, the model temperature increases monotonically from dusk to dawn meridian showing no dependence on radial distance.

As it follows from Equation 8 and Table 6, the near-Earth plasma sheet electron temperature increases with the solar wind velocity increase. Although there is only one coefficient associated with V_{SW}^* in Equation 8, the electron temperature response to V_{SW}^* increase is not uniform since the left part of Equation 8 is raised to the power of 2.3 ($A_9 = 2.3$ see Table 6). It means that the response is stronger on the dawn side where the electron temperature is higher.

The electron temperature increases with the southward IMF component increase. This effect is strongest near the midnight and disappears at the dawn and dusk MLTs. It

leads to the temperature peak localization in the midnight – dawn sector (See Figures 10d and 10f). The increase of IMF B_S leads to a shift of the temperature maximum from the dawn sector towards midnight. The post-midnight location of the electron temperature peak is probably related to the substorm activity (hot electrons drift eastward from an injection place in pre-midnight sector).

The electron temperature response to the northward IMF component (integrated over 2 hours) is negative and strongest at the outer border of the region. Figure 10e demonstrates the cooling of the electrons in the outer part of the region during the prolonged periods of northward IMF. It is probably related to the arrival of the cold magnetosheath plasma during the intervals of the northward IMF [*Wing et al.*, 2005; *Wang et al.*, 2007, 2010].

7. Discussion of the Model Performance

Figures 8a and 9a present the scatter plots of the model predictions versus real THEMIS observations (primary data set) for electron density and temperature models, respectively. The correlation coefficients between the model and the data were 0.82 for electron density and 0.75 for electron temperature models. Table 7 shows the correlation coefficients between the model predictions and the real data (primary data set) computed for every spatial bin separately. The root-mean-square deviations (RMS) and mean absolute deviations (MAD) are also shown. It can be seen that both models show their best performance on the dawnside of the region. It is not immediately clear what causes such asymmetry. Since the electrons undergo eastward magnetic drifts, their drift trajectories are expected to be regular on the dawnside, in contrast to the duskside where the drift paths can bifurcate (especially in the near-Earth region). Substorm activity is typically

peaked at the pre-midnight sector (and this distortion can become even stronger during the storm periods) and it can also contribute to the poorer performance of the model on the duskside.

However, a model performance estimation using the same data the models has been fitted to can not be considered as an independent test. The auxiliary data set (see Section 3) has not been used for the model coefficients determination. Indeed, it can be considered as an almost independent data set because only 26% of its data have the "neighbours" from primary data set within ±30 min (these neighbours are typically measurements on other probes). In addition, 20% of the auxiliary data set are referred to the early period of the THEMIS mission (2007–2009) which is not included in the primary data set. This theoretically allows us to check if there is any bias in the primary data set related to the detectors degradation. On the other hand, the auxiliary data set represents unaveraged $\sim$ 3-sec resolution measurements and we expect more noise in this data set and, hence, poorer correlations. Finally, the auxiliary data set is three times smaller than the primary data set and one can not expect that the model coefficients obtained by fitting the model to the smaller data set are of the same accuracy level.

Table 8 shows the correlation coefficients and the average deviations between the model and the auxiliary data set. Although the correlation coefficients are lower than those for the primary data set, they are still higher than 0.7 (typical correlation for the empirical models of the near-Earth plasma environment [*Tsyganenko and Mukai*, 2003; *Sergeev et al.*, 2015]). Strangely enough, the density model shows better agreement with auxiliary data set on the dusk side but it might be an effect of limited statistics. The scatter plots of the model prediction versus the data from auxiliary data set are presented in

Figures 8b and 9b. It can be seen that during high density periods, the models tend to underestimate the density values for significant number of events. Although this feature can be also noticed in Figures 8a for the primary data set, it is much more prominent in Figure 8b. To rule out possibility that this difference between two data sets is due to the detectors degradation, we inspected the data corresponding to these problematic points. It turned out that only 11% of these data are referred to the years 2007–2009, indicating that there is another reason of this discrepancy. We also checked the hypothesis that this bias is caused by transient processes in the plasma sheet called bursty bulk flows [*Angelopoulos et al.*, 1992; *Baumjohann et al.*, 1990]. However, the occurrence of events with the ion flow velocity exceeding 100 km/s for the problematic points is similar to that for the points near the diagonal of Figure 8b.

Finally, to test the model coefficient sensitivity to the change of the data set, we fitted the models to the auxiliary data set. The resulting coefficients are presented in the bottom part of Table 6. It can be seen that the difference between the density model coefficients obtained by fitting to the different data set can be as large as factor 3 (see A_3, A_4 coefficients). However, the difference between polynomials $A_1 + A_2R^* + A_3\phi^{*2}R^* + A_4\phi^{*2}$ (first four terms in Equation 5) is within 40%. The coefficients are not so different for the temperature model.

Comparison of our models performance with other empirical models is not straightforward. On one hand, our electron density model shows the best correlations between the model predictions and the data among all existing empirical models. On the other hand, such an evaluation of the model performance is strongly biased. The regions of applicability of our model and the models of other authors overlap only partly. The different

data sets were used for the construction of the models. Our data set includes storm-time intervals. The solar wind driving parameters undergo stronger variations during storm periods and all dependencies can be tracked more easily. On the other side, these highly disturbed periods obviously add more scatter to the data.

The correlation of the *Tsyganenko and Mukai* [2003] ion temperature model predictions with the data is comparable with that for our model for electron temperature (0.71 versus 0.75, respectively). The comparison of the ion and electron models seems to be justified because the ion and electron temperatures are highly correlated in the central plasma sheet [*Baumjohann et al.*, 1989]. It should be mentioned that the correlations in the *Tsyganenko and Mukai* [2003] study were computed for the whole region of the models applicability. Since the *Tsyganenko and Mukai* [2003] model covers the magnetotail between r = 10–$50R_E$, and the ion temperature reveals a stable increase with distance, a simple comparison of the correlations for the whole data sets puts the *Tsyganenko and Mukai* [2003] model in the more favorable conditions. On the other hand, the highly dynamic bursty bulk flows occur more frequently in the distant plasma sheet [*Baumjohann et al.*, 1990]. In addition, *Runov et al.* [2015] found that the correlation between the ion and electron temperatures disappears at $r < 12R_E$ and *Artemyev et al.* [2011] found that the relation between the electron and ion temperatures is non-linear in the mid-tail.

For development in the future, we foresee the following possibilities: (1) A presence of the multiple population components (cold, hot) should be addressed; (2) The inclusion of the geomagnetic activity indices as input parameters will increase the model accuracy; (3) Expansion of the dataset including non-storm periods.

8. Conclusions

The empirical models of the plasma sheet electron temperature and density on the nightside for $6R_E < r < 11R_E$ has been constructed using the data of the THEMIS mission obtained during the geomagnetic storm periods. The models depend on spatial coordinates as well as on the interplanetary medium parameters. The reader can find the codes for both models as well as procedures for the input parameters computation in the supplemental materials.

The model performances have been essentially improved by using lagged and time averaged solar wind parameters as model inputs. The best time-lag and duration of averaging were different for different parameters as well as showed some dependence on MLT (the latter feature is not included in the current model version).

It was found that the plasma sheet electron density equatorial distribution is symmetric with respect to the midnight meridian. It reveals a strong earthward gradient and a moderate symmetric variation with MLT. The plasma sheet density dependence on the external driving is parameterized by the solar wind proton density (averaged over preceding 4 hours) and southward IMF component (averaged over preceding 6 hours). In agreement with results of previous studies, the solar wind proton density is the main controlling parameter but the IMF B_S becomes of almost the same importance in the near-Earth region. The model density shows a positive response to the increase of either input parameter. The electron density revealed better correlation with IMF B_S averaged over the time interval which is closer to the geomagnetic storm main phase ($\sim$ 6 hours) rather than the substorm growth phase ($\sim$ 45 minutes). The root-mean-square deviation between the observed and predicted plasma sheet density values is 0.23 cm^{-3} and the

correlation coefficient is 0.82, the highest correlation with the data set ever obtained for these kinds of empirical models.

The electron temperature model is highly asymmetric with respect to the local midnight. The electron temperature maximum is located in the post-midnight – morning MLT sector. The model is parameterized by solar wind velocity and southward and northward components of IMF. The solar wind velocity is a major controlling parameter and the importance of B_S and B_N is comparable. The plasma sheet electron temperature responds positively to the solar wind velocity and IMF B_S increase and it responds negatively to the IMF B_N increase. In contrast to the density model, the electron temperature shows higher correlation with the southward IMF component when IMF B_S is averaged over preceding $\sim$45 min (substorm growth phase time scale). The effect of the northward component is parameterized by $\sim$ 2 hour average of IMF B_N. The impact of the prolonged IMF B_N manifests mostly in the outer part of the modelled region ($r > 8R_E$) while the influence of the IMF B_S is maximal in the midnight – post-midnight MLT sector. The correlation coefficient between the observed and predicted plasma sheet electron temperature values is 0.76 and the root-mean-square deviation is 2.6 keV.

The both models reveal the dawn-dusk asymmetry of their performances with better accuracy achieved in the dawn MLT sector. The correlations between the model predictions and observations vary between C.C.>0.7 in the dawn MLT sector and C.C.= 0.5–0.7 in the dusk sector.

Acknowledgments.

The plasma moments were obtained from the THEMIS mission web site (http://themis.ssl.berkeley.edu/index.shtml). The solar wind and IMF data were

downloaded from the OMNI database from the GSFC/SPDF OMNIWeb interface at http://omniweb.gsfc.nasa.gov. The 1-min. resolution SYM-H index was provided by the World Data Center for geomagnetism, Kyoto (http://wdc.kugi.kyoto-u.ac.jp/). The part of the research done by N. Ganushkina and S. Dubyagin has received funding from the European Union Seventh Framework Programme (FP7/20072013) under grant agreement 606716 SPACESTORM and from the European Union Horizon 2020 Research and Innovation programme under grant agreement 637302 PROGRESS. N. Ganushkina thanks the International Space Science Institute in Bern, Switzerland, for their support of the international teams on "Analysis of Cluster Inner Magnetosphere Campaign data, in application the dynamics of waves and wave-particle interaction within the outer radiation belt" and "Ring current modeling: Uncommon Assumptions and Common Misconceptions".

References

Artemyev, A. V., Baumjohann, W., Petrukovich, A. A., Nakamura, R., Dandouras, I., and Fazakerley, A.: Proton/electron temperature ratio in the magnetotail, *Ann. Geophys.*, *29*, 2253–2257, doi:10.5194/angeo-29-2253-2011, 2011.

Artemyev, A. V., Petrukovich, A. A., Nakamura, R., and Zelenyi, L. M. (2013), Profiles of electron temperature and Bz along Earth's magnetotail, *Ann. Geophys.*, *31*, 1109–1114, doi:10.5194/angeo-31-1109-2013.

Auster, H. U., et al. (2008), The THEMIS fluxgate magnetometer, *Space Sci. Rev.*,, *141*, 235–236, doi: 10.1007/s11214-008-9365-9.

Angelopoulos, V., W. Baumjohann, C. F. Kennel, F. V. Coroniti, M. G. Kivelson, R. Pellat, R. J. Walker, H. Lühr, and G. Paschmann (1992), Bursty bulk flows in the inner central plasma sheet, *J. Geophys. Res.*, *97(A4)*, 4027-4039, doi:10.1029/91JA02701.

Angelopoulos, V. (2008a), The THEMIS mission, *Space Sci. Rev.*, *141*, 5–34, doi:10.1007/s11214-008-9336-1.

Angelopoulos, V, D. Sibeck, C.W. Carlson, et al. (2008b), First Results from the THEMIS mission, *Space Sci. Rev.*, *141*, 453–476.

Baumjohann, W., G. Paschmann, and C. A. Cattell (1989), Average plasma properties in the central plasma sheet, *J. Geophys. Res.*, *94(A6)*, 6597-6606, doi:10.1029/JA094iA06p06597.

Baumjohann, W., G. Paschmann, and H. Lühr (1990), Characteristics of high-speed ion flows in the plasma sheet, *J. Geophys. Res.*, *95(A4)*, 3801-3809, doi:10.1029/JA095iA04p03801.

Borovsky, J. E., M. F. Thomsen, and R. C. Elphic (1998a), The driving of the plasma sheet by the solar wind, *J. Geophys. Res.*, *103(A8)*, 17617-17639, doi:10.1029/97JA02986.

Borovsky, J. E., M. F. Thomsen, R. C. Elphic, T. E. Cayton, and D. J. McComas (1998b), The transport of plasma sheet material from the distant tail to geosynchronous orbit, *J. Geophys. Res.*, *103(A9)*, 20297-20331, doi:10.1029/97JA03144.

Burin des Roziers, E., X. Li, D.N. Baker, T.A. Fritz, R. Friedel, T.G. Onsager, and I. Dandouras (2009), Energetic plasma sheet electrons and their relationship with the solar wind: A cluster and geotail study, *J. Geophys. Res.*, *114*, A02220, DOI: 10.1029/2008JA013696.

Chen Y., R. H. W. Friedel, G. D. Reeves, PSD distributions of energetic electrons in the outer radiation belt during two Geospace Environment Modeling Inner Magnetosphere/Storms selected storms, *J. Geophys. Res.*, *111*, A11S04, doi:10.1029/2006JA011703, 2006.

Davis, V. A., M. J. Mandell, and M. F. Thomsen (2008), Representation of the measured geosynchronous plasma environment in spacecraft charging calculations, *J. Geophys. Res.*, *113*, A10204, doi:10.1029/2008JA013116.

Denton, M. H., M. F. Thomsen, H. Korth, S. Lynch, J. C. Zhang, and M. W. Liemohn (2005), Bulk plasma properties at geosynchronous orbit, *J. Geophys. Res.*, *110*, A07223, doi:10.1029/2004JA010861.

Denton, M. H., M. F. Thomsen, V. K. Jordanova, M. G. Henderson, J. E. Borovsky, J. S. Denton, D. Pitchford, and D. P. Hartley (2015), An empirical model of electron and ion fluxes derived from observations at geosynchronous orbit, *Space Weather*, *13*, doi:10.1002/2015SW001168.

Dubyagin, S., V. Sergeev, S. Apatenkov, V. Angelopoulos, R. Nakamura, J. McFadden, D. Larson, and J. Bonnell (2010), Pressure and entropy changes in the flow-braking region during magnetic field dipolarization, *J. Geophys. Res.*, *115*, A10225, doi:10.1029/2010JA015625.

Friedel, R. H. W., H. Korth, M. G. Henderson, M. E. Thomsen, J. D. Scudder (2001), Plasma sheet access to the inner magnetosphere, *J.* Geophys. Res., *1*06, 5845-5858.

Jordanova, V. K., and Y. S. Miyoshi (2005), Relativistic model of ring current and radiation belt ions and electrons: Initial results, *Geophys. Res. Lett.*, *32*, L14104, doi:10.1029/2005GL023020.

Jordanova, V. K., Y. Yu, J. T. Niehof, R. M. Skoug, G. D. Reeves, C. A. Kletzing, J. F. Fennell, and H. E. Spence (2014), Simulations of inner magnetosphere dynamics with an expanded RAM-SCB model and comparisons with Van Allen Probes observations, *Geophys. Res. Lett.*, *41*, 2687-2694, doi:10.1002/2014GL059533.

Ganushkina N. Yu., O. Amariutei, Y. Y. Shpritz, and M. Liemohn (2013), Transport of the plasma sheet electrons to the geostationary distances, *J.* Geophys. Res., *118*, doi:10.1029/2012JA017923.

Ganushkina N. Yu., M. Liemohn, O. Amariutei, and D. Pitchford (2013b), Low energy electrons (5-50 keV) in the inner magnetosphere, *J.* Geophys. Res., 119, 246259, doi:10.1002/2013JA019304.

Ganushkina, N. Y., O. A. Amariutei, D. Welling, and D. Heynderickx, (2015), Nowcast model for low-energy electrons in the inner magnetosphere, *S*pace Weather, *1*3, 1634, doi:10.1002/2014SW001098.

Garrett, H. B. (1981), The charging of spacecraft surfaces, *R*ev. Geophys., *1*9(4), 577, doi:10.1029/RG019i004p00577.

Kaufmann, R. L., W. R. Paterson, and L. A. Frank (2005), Relationships between the ion flow speed, magnetic flux transport rate, and other plasma sheet parameters, *J.* Geophys. Res., *1*10, A09216, doi:10.1029/2005JA011068.

Kerns, K. J., D. A. Hardy, and M. S. Gussenhoven, Modeling of convection boundaries seen by CRRES in 120-eV to 28-keV particles, *J.* Geophys. Res., *9*9, 2403, 1994.

Korth, H., M. F. Thomsen, J. E. Borovsky, and D. J. McComas (1999), Plasma sheet access to geosynchronous orbit, *J.* Geophys. Res., *1*04, 25,047-25,061.

Kurita, S., Y. Miyoshi, F. Tsuchiya, Y. Nishimura, T. Hori, Y. Miyashita, T. Takada, A. Morioka, V. Angelopoulos, J. P. McFadden, H. U. Auster, J. M. Albert, V. Jordanova, and H. Misawa et al. (2011), Transport and loss of the inner plasma sheet electrons: THEMIS observations, *J.* Geophys. Res., *1*16, A03201, doi:10.1029/2010JA015975.

Lanzerotti, L. J., K. LaFleur, C. G. Maclennan, and D. W. Maurer (1998), Geosynchronous spacecraft charging in January 1997, *Geophys. Res. Lett.*, *25(15)*, 2967-2970.

Liemohn, M. W., G. V. Khazanov, and J. U. Kozyra (1998), Banded electron structure formation in the inner magnetosphere, *G*eophys. Res. Lett., *2*5, 877.

Mauk, B. H., and C.-I. Meng (1983), Characterization of geostationary particle signatures based on the "Injection Boundary" model, *J.* Geophys. Res., *8*8, 3055.

McFadden, J. P., Carlson, C. W., Larson, D., Angelopoulos, V., Ludlam, M., Abiad, R., Elliott, B., Turin, P., Marckwordt, M. (2008), The THEMIS ESA plasma instrument and in-flight calibration, *Space Sci. Rev., 141*, 277–302, doi: 10.1107/s11214-008-9440-2

McFadden, J.P., Carlson, C.W., Larson, D., Bonnell, J., Mozer, F., Angelopoulos, V., Glassmeier, K.-H., Auster, U. (2008), THEMIS ESA first science results and performance issues, *Space Sci. Rev., 141*, 477–508, doi:10.1007/s11214-008-9433-1.

Miyoshi, Y. S., V. K. Jordanova, A. Morioka, M. F. Thomsen, G. D. Reeves, D. S. Evans, and J. C. Green (2006), Observations and modeling of energetic electron dynamics during the October 2001 storm, *J.* Geophys. Res., *111*, A11S02, doi:10.1029/2005JA011351.

Nelder, John A.; R. Mead (1965), A simplex method for function minimization, *Computer Journal*, *7*, 308-313, doi:10.1093/comjnl/7.4.308

Runov, A., V. Angelopoulos, C. Gabrielse, J. Liu, D. L. Turner, and X.-Z. Zhou (2015), Average thermodynamic and spectral properties of plasma in and around dipolarizing flux bundles. *J. Geophys. Res. Space Physics*, *120*, 4369-4383, doi:10.1002/2015JA021166.

Sergeev, V. A., N. P. Dmitrieva, N. A. Stepanov, D. A. Sormakov, V. Angelopoulos, and A. V. Runov (2015), On the plasma sheet dependence on solar wind and substorms

and its role in magnetosphere-ionosphere coupling. *Earth, Planets and Space*, *67*, doi: 10.1186/s40623-015-0296-x.

Shukhtina, M. A., N. P. Dmitrieva, N. G. Popova, V. A. Sergeev, A. G. Yahnin, and I. V. Despirak (2005), Observational evidence of the loading-unloading substorm scheme, *Geophys. Res. Lett.*, *32*, L17107, doi:10.1029/2005GL023779.

Sicard-Piet, A., S. Bourdarie, D. Boscher, R. H. W. Friedel, M. Thomsen, T. Goka, H. Matsumoto, and H. Koshiishi (2008), A new international geostationary electron model: IGE-2006, from 1 keV to 5.2 MeV, *Space Weather*, *6*, S07003, doi:10.1029/2007SW000368.

Terasawa, T., M. Fujimoto, T. Mukai, I. Shinohara, Y. Saito, T. Yamamoto, S. Machida, S. Kokubun, A. J. Lazarus, J. T. Steinberg, and R. P. Lepping (1997), Solar wind control of density and temperature in the near-Earth plasma sheet: WIND/GEOTAIL collaboration, *Geophys. Res. Lett.*, *24*, 8, 935-938, doi: 10.1029/96GL04018.

Thomsen, M. F., M. G. Henderson, and V. K. Jordanova (2013), Statistical properties of the surface-charging environment at geosynchronous orbit, *Space Weather*, *11*, 237244, doi:10.1002/swe.20049.

Tsyganenko, N. A., and T. Mukai (2003), Tail plasma sheet models derived from Geotail particle data, *J. Geophys. Res.*, *108*, 1136, doi:10.1029/2002JA009707, A3.

Tsyganenko, N. A., and D. H. Fairfield (2004), Global shape of the magnetotail current sheet as derived from Geotail and Polar data, *J. Geophys. Res.*, *109*, A03218, doi:10.1029/2003JA010062.

Wang, C.-P., L. R. Lyons, J. M. Weygand, T. Nagai, and R. W. McEntire (2006), Equatorial distributions of the plasma sheet ions, their electric and magnetic drifts, and

magnetic fields under different interplanetary magnetic field Bz conditions, *J. Geophys. Res.*, *111*, A04215, doi:10.1029/2005JA011545.

Wang, C.-P., L. R. Lyons, T. Nagai, J. M. Weygand, and R. W. McEntire (2007), Sources, transport, and distributions of plasma sheet ions and electrons and dependences on interplanetary parameters under northward interplanetary magnetic field, *J. Geophys. Res.*, *112*, A10224, doi:10.1029/2007JA012522.

Wang, C.-P., L. R. Lyons, T. Nagai, J. M. Weygand, and A. T. Y. Lui (2010), Evolution of plasma sheet particle content under different interplanetary magnetic field conditions, *J. Geophys. Res.*, *115*, A06210, doi:10.1029/2009JA015028.

Wang, C.-P., M. Gkioulidou, L. R. Lyons, and V. Angelopoulos (2012), Spatial distributions of the ion to electron temperature ratio in the magnetosheath and plasma sheet, *J. Geophys. Res.*, *117*, A08215, doi:10.1029/2012JA017658.

Wing, S., and P. T. Newell, 2D plasma sheet ion density and temperature profiles for northward and southward IMF, *Geophys. Res. Lett.*, *29(9)*, doi:10.1029/2001GL013950, 2002.

Wing, S., J. R. Johnson, P. T. Newell, and C.-I. Meng (2005), Dawn-dusk asymmetries, ion spectra, and sources in the northward interplanetary magnetic field plasma sheet, *J. Geophys. Res.*, *110*, A08205, doi:10.1029/2005JA011086.

Åsnes, A., R. W. H. Friedel, B. Lavraud, G. D. Reeves, M. G. G. T. Taylor, and P. Daly (2008), Statistical properties of tail plasma sheet electrons above 40 keV, *J.* Geophys. Res., *1*13, A03202, doi:10.1029/2007JA012502.

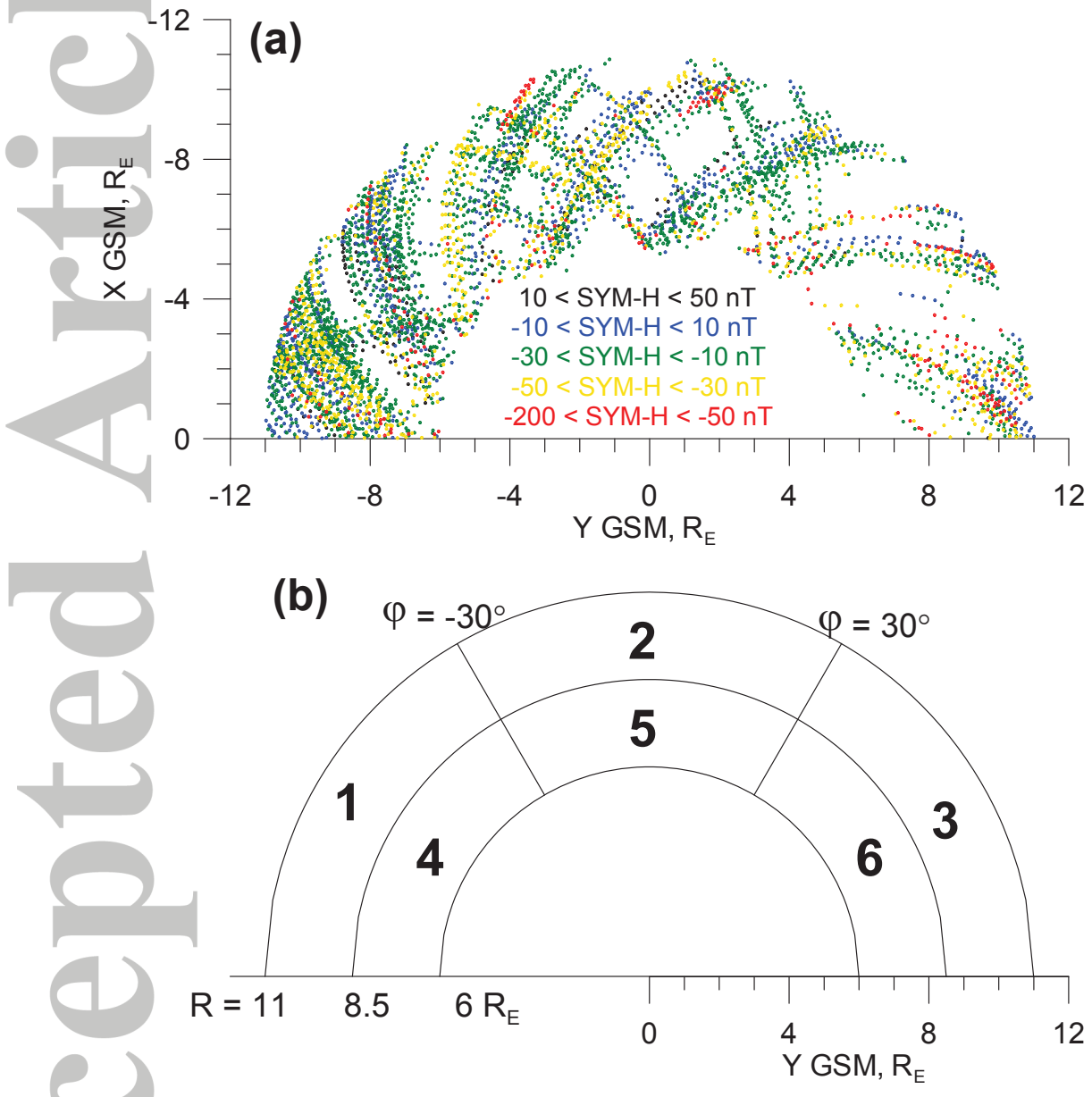

Figure 1. (a) Spatial coverage of the equatorial magnetosphere by THEMIS observations. Only every tenth point is shown. Color shows corresponding SYM-H. (b) Spatial bins numeration.

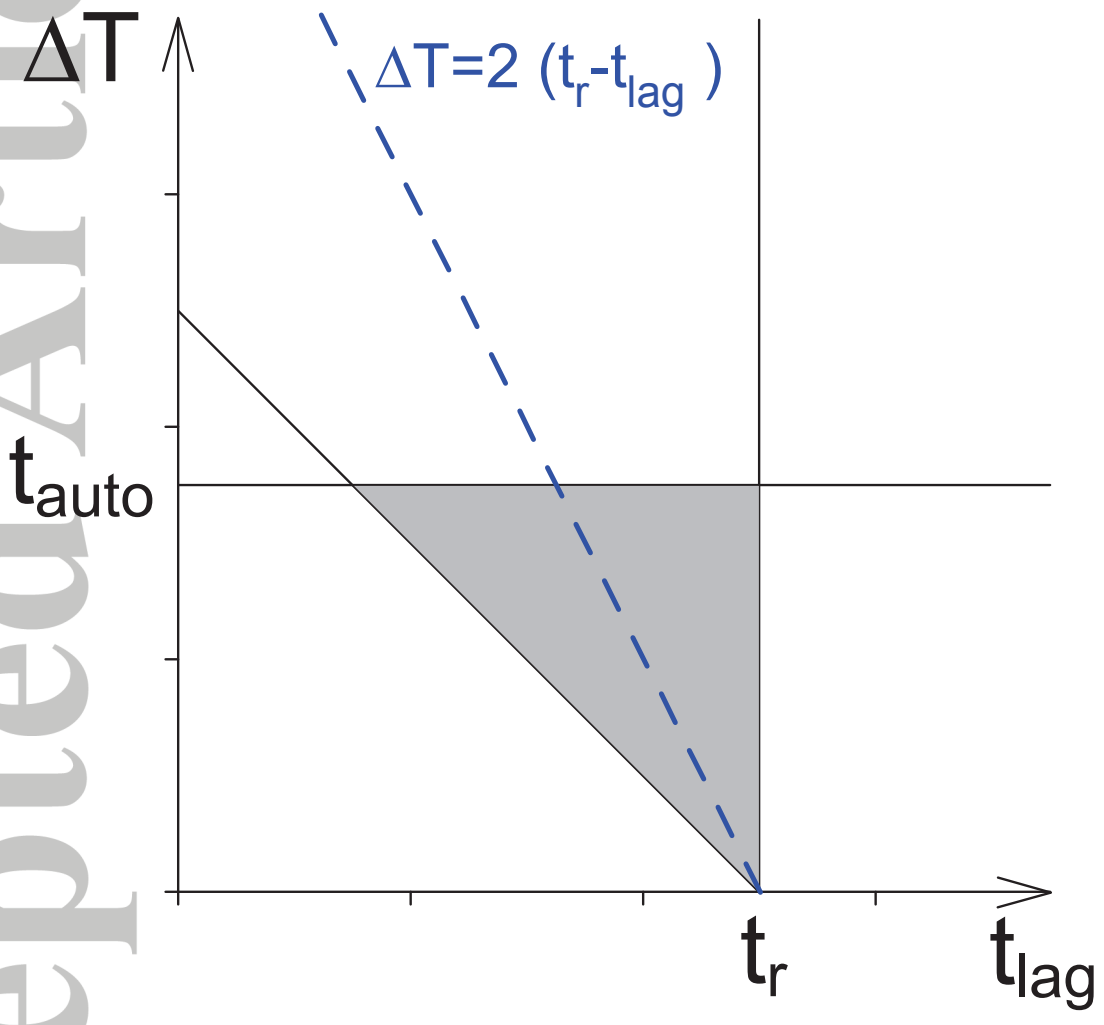

Figure 2. Sketch explaining how to interpret Figures 3–7. The horizontal axis represents the time lag and the vertical axis represents duration of averaging. See explanation in the text.

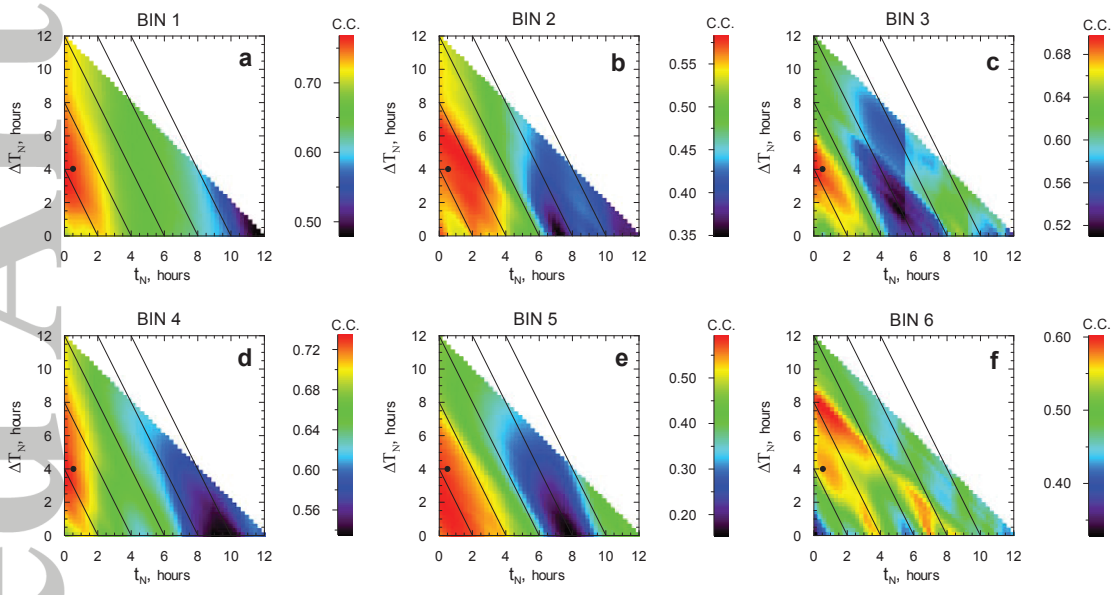

Figure 3. Correlation coefficients (color coded) between the plasma sheet electron density and the solar wind density for six regions of the magnetotail. Vertical and horizontal axes show the solar wind density average duration and the lag of the solar wind density observations with respect to plasma sheet measurements. The oblique lines show $\Delta T_N = const - 2 \cdot t_N$ dependencies. The black filled circles mark ΔT_N and t_N which are used for the input parameters computation.

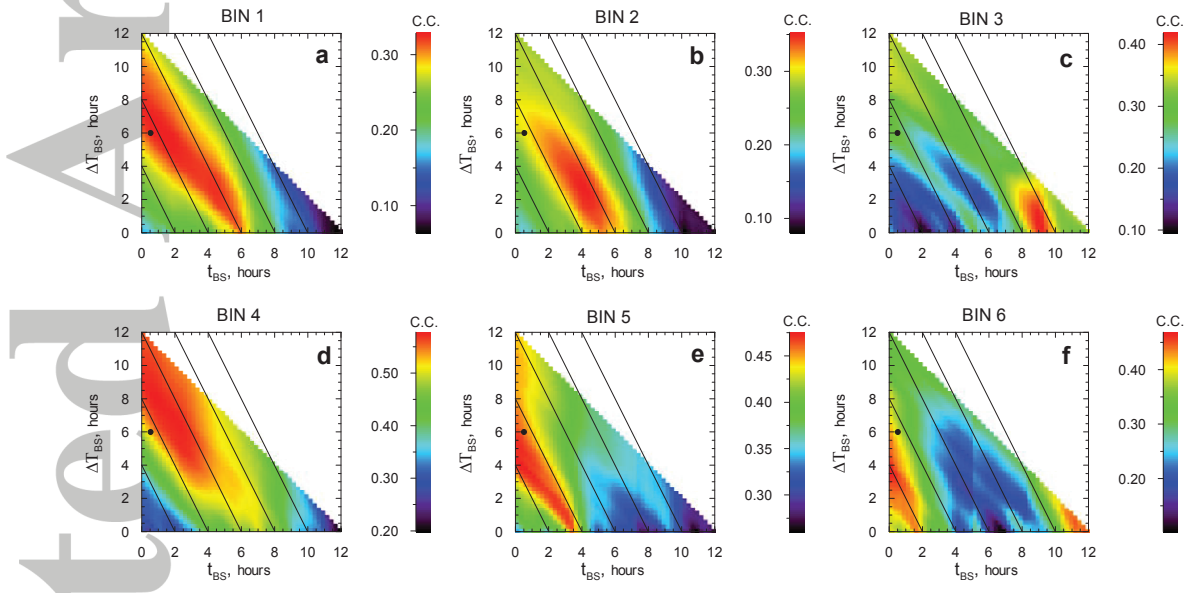

Figure 4. The same as Figure 3 but for correlation coefficients between the plasma sheet electron density and the southward component of IMF B_Z.

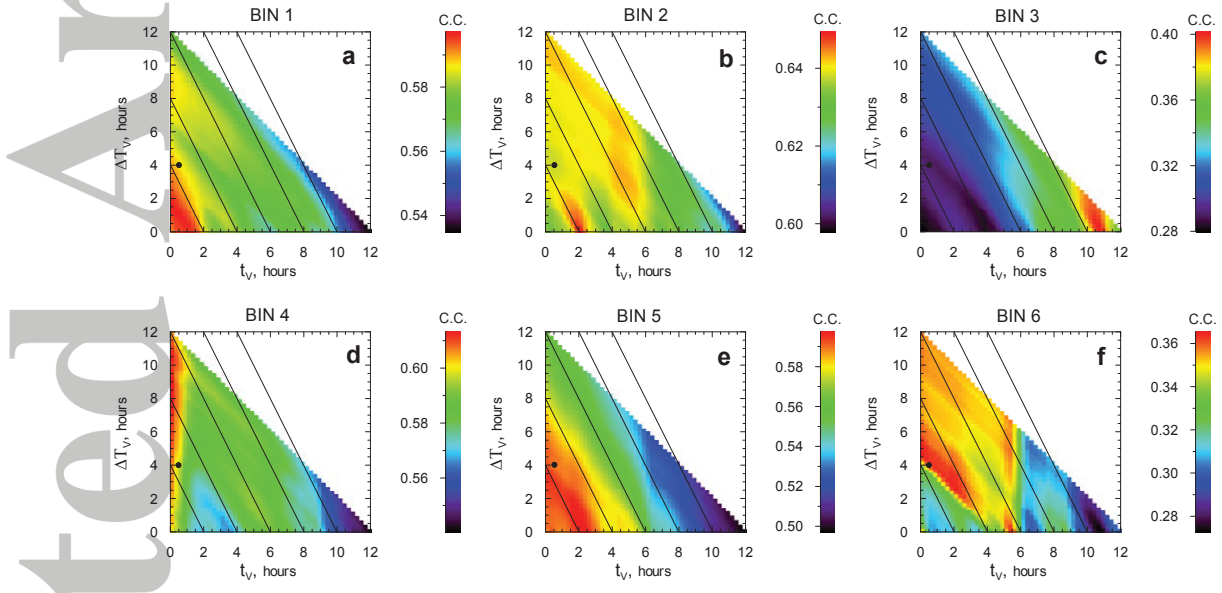

Figure 5. The same as Figure 3 but for correlation coefficients between the plasma sheet electron temperature and the solar wind velocity.

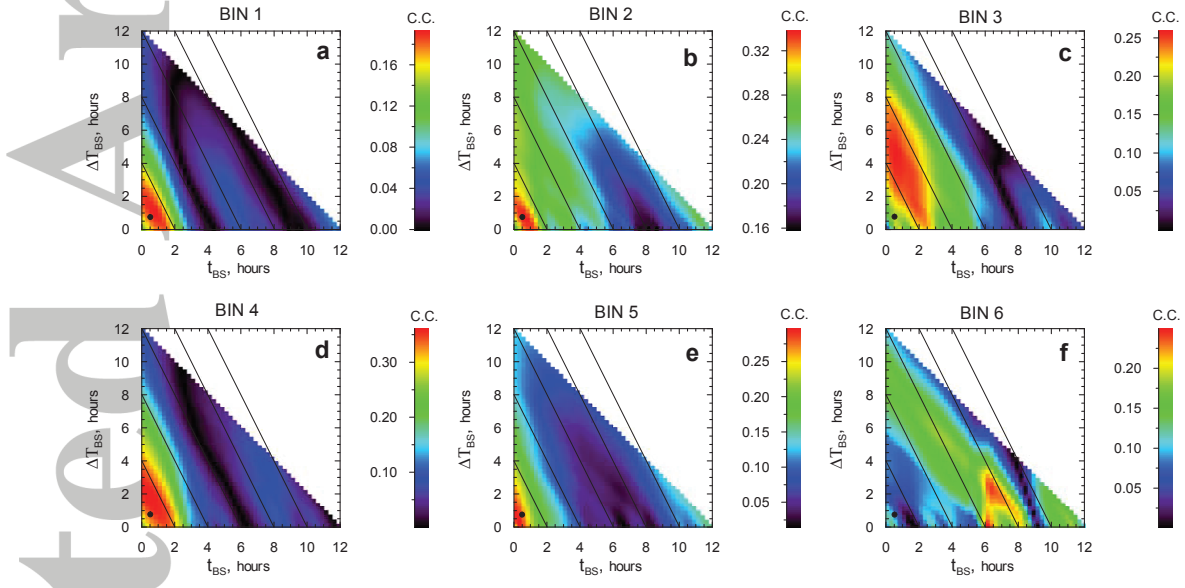

Figure 6. The same as Figure 3 but for correlation coefficients between the plasma sheet electron temperature and southward component of IMF B_Z.

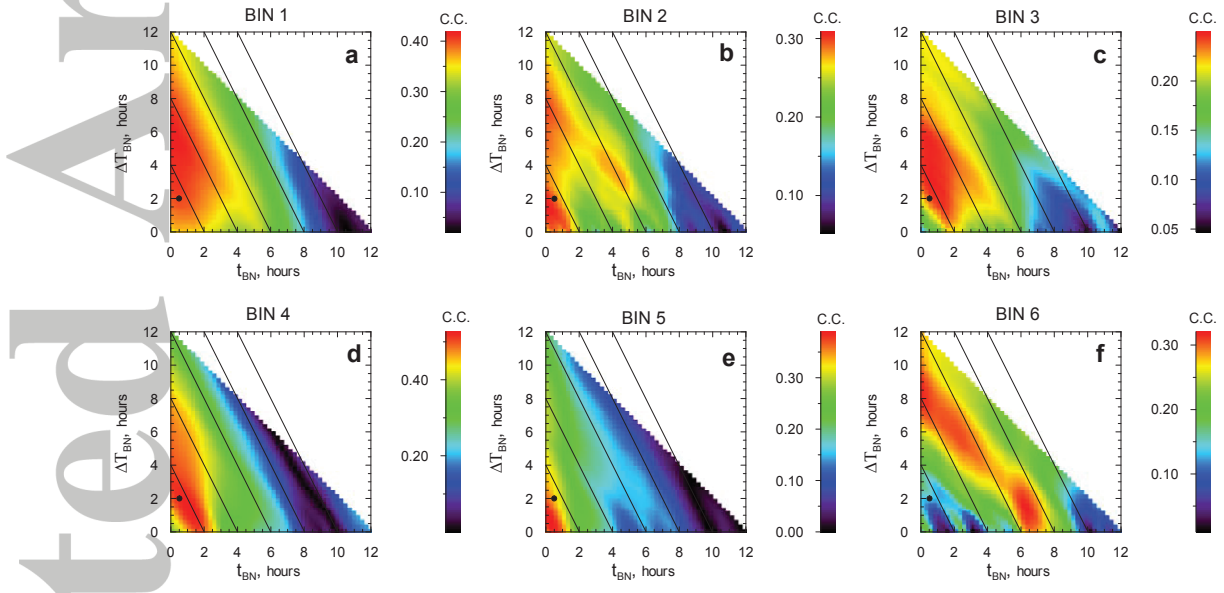

Figure 7. The same as Figure 3 but for correlation coefficients between the plasma sheet electron temperature and the northward component of IMF B_Z.

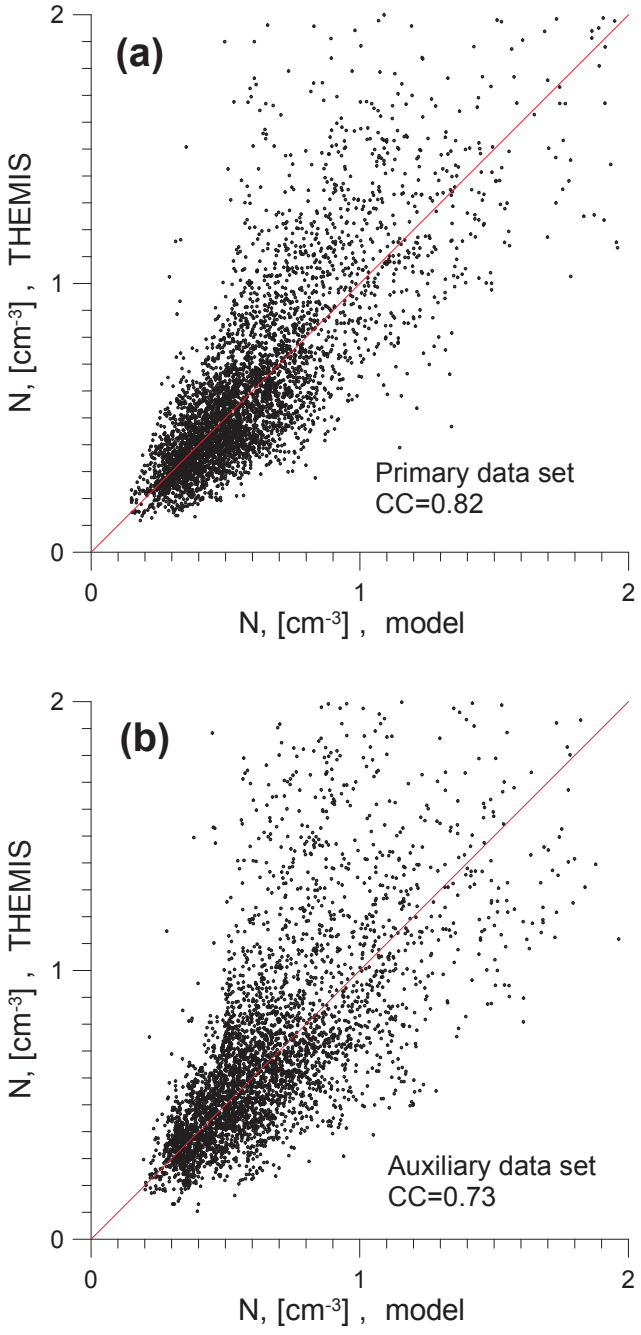

Figure 8. Plasma sheet electron density predicted by the empirical model versus that measured by the THEMIS probes. (a) The THEMIS measurements are represented by primary data set. Every tenth point is shown. (b) The THEMIS measurements are represented by auxiliary data set. Every third point is shown.

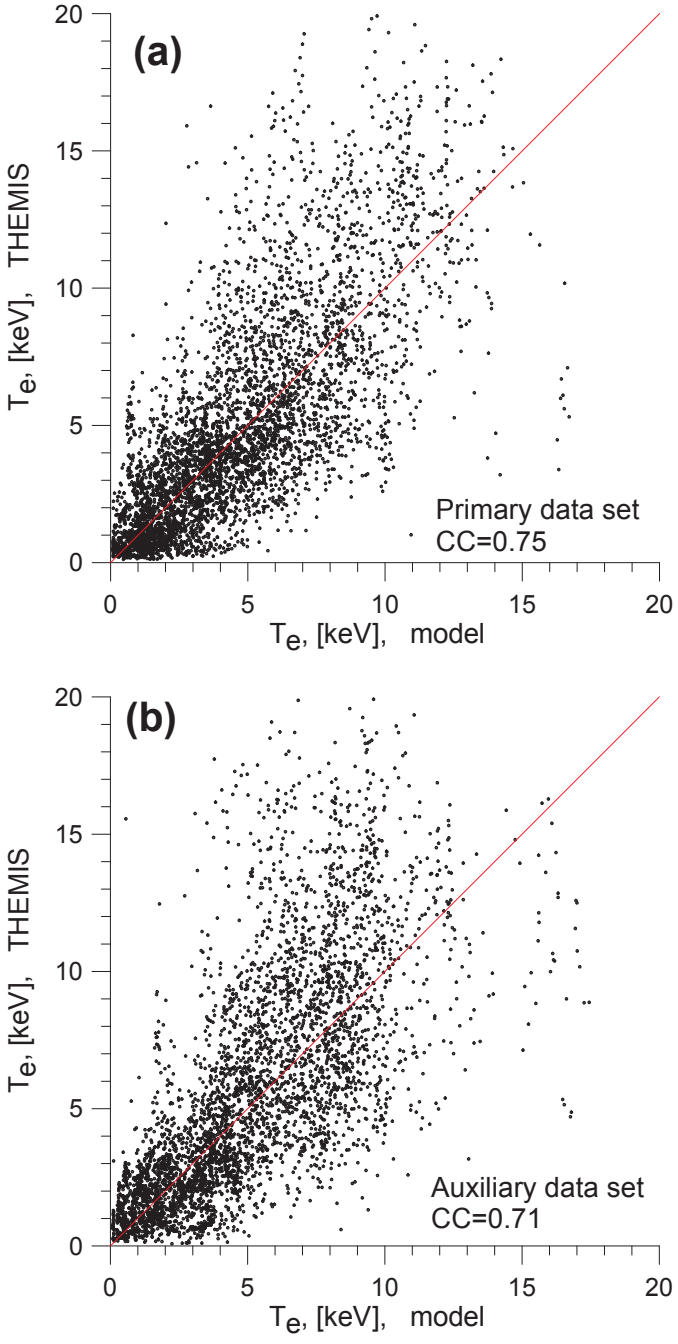

Figure 9. The same as Figure 8 but for the electron temperature model.

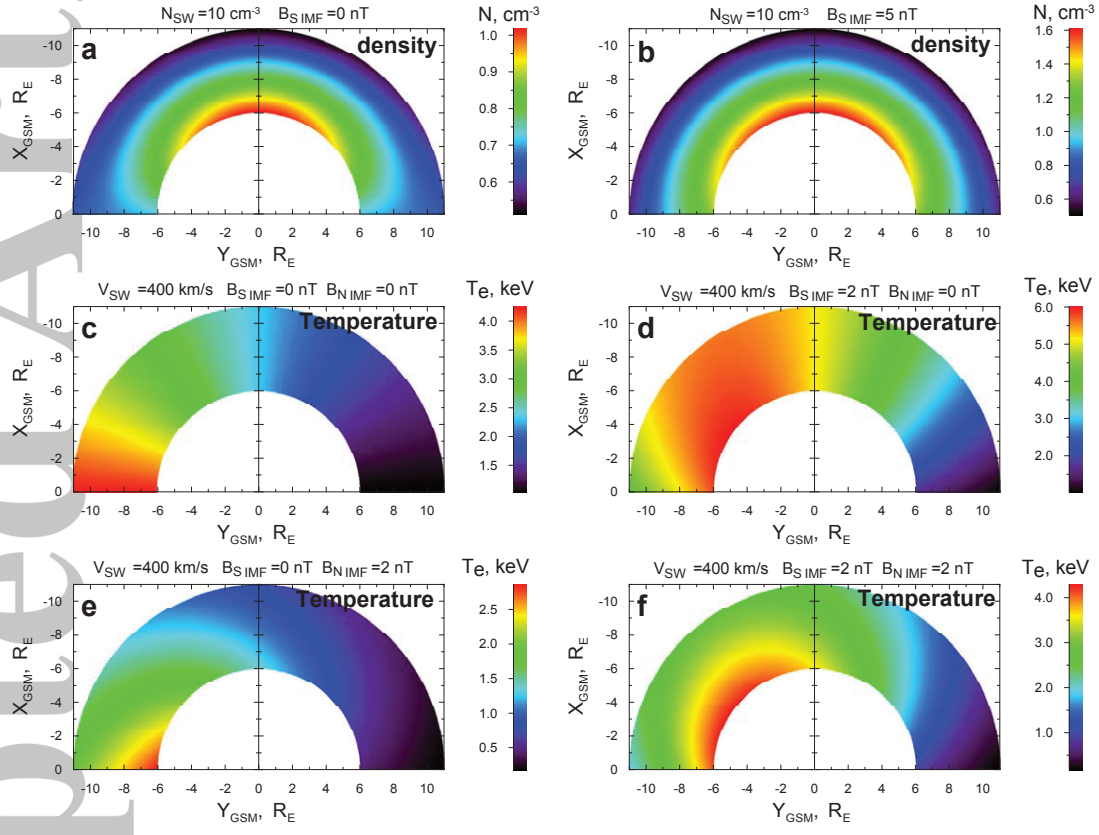

Figure 10. Distributions of the electron temperature and density in the equatorial plane. (a–b) density model, (c–f) electron temperature model.

Table 1. Distribution of the number of the samples over the THEMIS mission period for primary and auxiliary data sets.

Years	2007	2008	2009	2010	2011	2012	2013
# primary	0	0	0	7475	11347	12693	13486
# auxiliary	1992	583	38	1688	2033	2520	3317

Table 2. Statistical properties of the data sets for different spatial bins. Top part is for standard deviations of instant values corresponding to the zero lag, and the bottom part shows the ranges of standard deviations found for lags between 0 and 12 h.

Bin index	1	2	3	4	5	6
r, $[R_E]$	8.5–11	8.5–11	8.5–11	6–8.5	6–8.5	6–8.5
ϕ	$-90°$–$-30°$	$-30°$–$30°$	$30°$–$90°$	$-90°$–$-30°$	$-30°$–$30°$	$30°$–$90°$
#	16257	9046	4698	6780	5812	2295
σN_{SW}, [cm^{-3}]	5.1	3.7	5.1	6.0	4.3	3.5
σV_{SW}, km/s	118	109	88	112	110	93
σB_{ZIMF}, nT	4.0	3.9	4.0	4.4	3.9	3.6
σN_{SW}, [cm^{-3}]	4.6-6.3	3.6-5.2	3.3-5.1	5.7-9.6	3.3-8.4	3.0-4.6
σV_{SW}, km/s	117-121	106-111	88- 95	110-118	108-114	90- 98

Table 3. Correlations of the plasma sheet electron density with the solar wind parameters. Top part is for instant values $t_0 - 45$ min. and the bottom part shows best correlations found for all lags and durations of averaging.

Bin index	1	2	3	4	5	6
N_{SW}	0.71	0.54	0.60	0.69	0.57	0.39
IMF B_S	0.18	0.20	0.16	0.28	0.38	0.36
IMF B_N	0.24	0.33	0.35	0.16	0.13	0.08
N_{SW}	0.77	0.58	0.70	0.73	0.59	0.60
IMF B_S	0.33	0.35	0.42	0.58	0.48	0.47
IMF B_N	0.28	0.35	0.46	0.18	0.20	0.22

Table 4. Correlations of the plasma sheet electron temperature with the solar wind parameters. Top part is for instant values $t_0 - 45$ min. and the bottom part shows best correlations found for all lags and durations of averaging.

Bin index	1	2	3	4	5	6
V_{SW}	0.59	0.63	0.28	0.59	0.59	0.31
IMF B_S	0.17	0.32	0.19	0.32	0.28	0.12
IMF B_N	-0.36	-0.29	-0.17	-0.42	-0.38	-0.23
V_{SW}	0.60	0.65	0.40	0.61	0.60	0.37
IMF B_S	0.19	0.34	0.26	0.36	0.30	0.25
IMF B_N	-0.42	-0.31	-0.25	-0.53	-0.39	-0.32

Table 5. Time constants for computation of the empirical models input parameters.

	t_N	ΔT_N	t_{BS}	ΔT_{BS}	t_V	ΔT_V	t_{BN}	ΔT_{BN}
Density	0.58 h	4.00 h	0.58 h	6.00 h				
Temperature			0.58 h	0.75 h	0.58 h	4.00 h	0.58 h	2.00 h

Table 6. Empirical model parameters.

	A_1	A_2	A_3	A_4	A_5	A_6	A_7	A_8	A_9
Density	1.23	-1.01	0.874	-0.820	0.392	0.521	-0.474		
Temperature	-0.0215	-0.426	1.47	0.587	-0.538	-0.489	0.32	0.36	2.31
Density[†]	1.01	-0.747	0.303	-0.248	0.362	0.498	-0.474		
Temperature[†]	-0.0922	-0.390	1.64	0.767	-1.02	-0.395	0.26	0.52	2.16

[†] Model coefficients obtained by fitting the model to the auxiliary data set.

Table 7. Characteristics of the empirical models quality. Top part of the table for the electron density model and the bottom one is for the temperature model

Bin index	all	1	2	3	4	5	6
C.C.	0.82	0.77	0.73	0.70	0.84	0.73	0.72
RMS, [cm^{-}3]	0.23	0.21	0.16	0.17	0.28	0.29	0.32
MAD, [cm^{-}3]	0.15	0.13	0.11	0.13	0.20	0.22	0.23
C.C.	0.75	0.72	0.72	0.65	0.79	0.75	0.54
RMS, [keV]	2.6	2.5	3.1	2.0	2.4	2.9	2.3
MAD, [keV]	1.8	1.8	2.1	1.3	1.8	2.1	1.7

Table 8. The same as Table 7 but for comparison with auxiliary data set. In addition, a number of data records for every bin is given in the second line.

Bin index	all	1	2	3	4	5	6
#	12171	5220	1211	1069	2922	1014	689
C.C.	0.73	0.61	0.70	0.70	0.63	0.79	0.80
RMS, [cm^{-}3]	0.28	0.27	0.18	0.19	0.34	0.32	0.28
MAD, [cm^{-}3]	0.19	0.16	0.12	0.14	0.25	0.23	0.21
C.C.	0.71	0.75	0.65	0.82	0.72	0.67	0.57
RMS, [keV]	3.1	2.4	3.6	3.7	2.9	4.3	4.2
MAD, [keV]	2.2	1.8	2.5	2.2	2.2	3.0	3.0